Journal of Power Sources 273 (2015) 1023–1029

Contents lists available at ScienceDirect

Journal of Power Sources

journal homepage: www.elsevier.com/locate/jpowsour

# Characterization, average and electronic structures during charge–discharge cycle in $0.6Li_2MnO_3–0.4Li(Co_{1/3}Ni_{1/3}Mn_{1/3})O_2$ solid solution of a cathode active material for Li-ion battery

Yasushi Idemoto [a, b, *], Ryosuke Kawai [a], Naoya Ishida [a, b], Naoto Kitamura [a, b]

[a] Department of Pure & Applied Chemistry, Faculty of Science & Technology, Tokyo University of Science, 2641 Yamazaki, Noda-shi, Chiba 278-8510, Japan
[b] Division of Ecosystem Research, Research Institute for Science and Technology, Tokyo University of Science, 2641 Yamazaki, Noda-shi, Chiba 278-8510, Japan

## HIGHLIGHTS

- We analyze the crystal and electronic structure of layered material.
- The site occupancy changed during charge/discharge cycles.
- The covalency increase in Li–O between the first and fifth charge processes.
- The Li at the 4*h* site is especially difficult to extract from the host materials.

## ARTICLE INFO

*Article history:*
Received 6 July 2014
Received in revised form
2 September 2014
Accepted 24 September 2014
Available online 2 October 2014

*Keywords:*
Li ion battery
Cathode
Average structure
Electronic structure

## ABSTRACT

The $0.6Li_2MnO_3–0.4Li(Co_{1/3}Ni_{1/3}Mn_{1/3})O_2$ solid solution was prepared by the co-precipitation method. The average structure analysis based on the Rietveld method using neutron diffraction was carried out. As a result, the charging process eliminated Li from the transition metal layer as well as the lithium layer, and the dominant elimination of Li was suggested to be from the 2*b* site (S.G.; *C*2/*m*). The amount of the cation mixing of Ni at the 2*c* site in the Li layer tended to increase from the first to fifth cycles. It was suggested that Co moved to the 4*g* site after discharge, but to the 2*b* site after charging. On the other hand, the opposite tendency was shown for Mn. In addition, an electronic-structure analysis based on the Maximum Entropy Method was carried out. The covalent linkage increased in 4*h*-4*i* and 4*h*-8*j* between the first and fifth charge processes. It was also found that most of the Li in the 4*h* site was not extracted at the fifth cycle compared to the first cycle.



## 1. Introduction

The transition metal oxide, $LiCoO_2$, has been developed as a cathode active material for the lithium ion battery in the past few decades. Recently, an alternative material with lower cobalt content which is less expensive and toxic is highly expected. As one of the promising candidates, lithium-rich transition-metal oxides, $xLi_2MnO_3–(1-x)Li(Mn, Co, Ni)O_2$, have drawn much attention. These materials achieve a relatively high specific capacity only after the initial charge beyond 4.5–4.6 V *vs.* $Li/Li^+$ along with a high irreversible capacity [1–7]. Some previous studies reported that this irreversible capacity resulted from the extraction of $O_2$ and/or $Li_2O$ from the cathode. The mechanism of an irreversible capacity has been extensively studied [1,5]. After the 1st discharge process, the high capacity was obtained by the redox of $LiMO_2$ (M = Mn, Ni, Co) and $LiMnO_2$. However, a significant irreversible capacity during the 1st charge process was observed and corresponded to the generation of oxygen which induced the capacity fading upon cycling [1]. On the other hand, there are many problems yet to be solved regarding the crystal structure. Although the main diffraction peaks of $xLi_2MnO_3–(1-x)Li(Mn, Co, Ni)O_2$ were attributed to the layered rock-salt structure with $R\bar{3}m$, the diffraction peaks in the two theta range of around 20°–23° were deduced from the $Li_2MnO_3$ domain with *C*2/*m* [8–11]. Various discussions have ensued about the transition metal arrangements with proposals of

* Corresponding author. Department of Pure & Applied Chemistry, Faculty of Science & Technology, Tokyo University of Science, 2641 Yamazaki, Noda-shi, Chiba 278-8510, Japan. Tel.: +81 4 7122 9493; fax: +81 4 7125 7761.
*E-mail addresses:* idemoto@rs.noda.tus.ac.jp, idemoto@rs.tus.ac.jp (Y. Idemoto).

http://dx.doi.org/10.1016/j.jpowsour.2014.09.157
0378-7753/

$LiMn_6$, $LiMn_5Ni$, and $LiMn_{6-x}M_x$ (M = Ni, Co) clusters [5–8]. The more complex transition metal arrangements, M = Mn, Ni, Co, have not been investigated in detail.

The electronic structure was also needed to reveal the initial electrochemical reaction for $xLi_2MnO_3$–$(1-x)$Li(Mn, Ni, Co)$O_2$. However, it is difficult to analyze the electronic structure by the Maximum Entropy Method (MEM) of the X-ray diffraction data for the electrode after its charge and/or discharge of a coin-sized cell. We have clarified the cation-mixing and oxygen amounts of $0.5Li_2MnO_3$–$0.5LiMn_xNi_xCo_{1-2x}O_2$ ($x = 1/3, 5/12$) by a reduced heat treatment of the material [12] and the crystal structure during the charge–discharge process of $LiNi_{0.8}Co_{0.19}Cu_{0.01}O_2$ using about 10 mg [13].

In this study, we investigated the average and electronic structures of the $0.6Li_2MnO_3$–$0.4Li(Co_{1/3}Ni_{1/3}Mn_{1/3})O_2$ solid solution, which has a high specific capacity, after charge and discharge of the first cycle and steady state, *i.e.*, at the fifth cycle, using the Rietveld analysis for neutron and synchrotron X-ray diffractions and the Maximum Entropy Method (MEM) analysis, respectively.

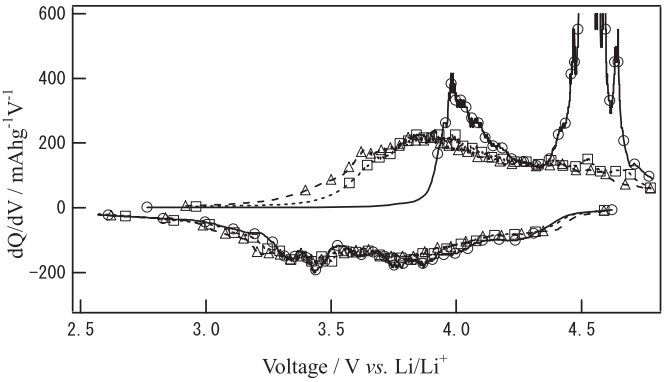


**Fig. 2.** Differential–capacity plots of the first and fifth charge/discharge profiles in $0.6Li_2MnO_3$–$0.4Li(Mn_{1/3}Ni_{1/3}Co_{1/3})O_2$. (Temperature: 25 °C, current density: 20 mA $g^{-1}$, cut off voltage: 2.5–4.8 V *vs.* Li/$Li^+$) ○: first cycle □: second cycle Δ: fifth cycle.

## 2. Experimental

### 2.1. Synthesis of samples

The pristine $0.6Li_2MnO_3$–$0.4Li(Co_{1/3}Ni_{1/3}Mn_{1/3})O_2$ was synthesized by a co-precipitation method. Stoichiometric amounts of $Co(NO_3)_2 \cdot 6H_2O$ (Wako Pure Chemical Industries, Ltd., 98%), $Mn(NO_3)_2 \cdot 6H_2O$ (Wako Pure Chemical Industries, Ltd., 98%) and $Ni(NO_3)_2 \cdot 6H_2O$ (Wako Pure Chemical Industries, Ltd., 98%) were dissolved in double-distilled water and dropped with the 0.5 mol $L^{-1}$ solution of $LiOH \cdot H_2O$. The precipitated powders were carefully filtered and washed, then dried in air at 100 °C overnight. The dried transition precursors were mixed with a stoichiometric amount of $LiOH \cdot H_2O$. The obtained precursors were heated at 650 °C for 15 h, then pressed into pellets. The pellets were calcined at 950 °C for 15 h and subsequently ground.

### 2.2. Characterization

Phase identification was carried out by powder X-ray diffraction (XRD, PANalytical X'Pert PRO diffractometer) using CuK$\alpha$ radiation operating at 45 kV and 40 mA. The lattice parameters were determined using a least square refinement method. The metal composition of the samples was analyzed using inductively coupled plasma (ICP) emission spectroscopy (ICPE-9000, Shimadzu, Ltd.).

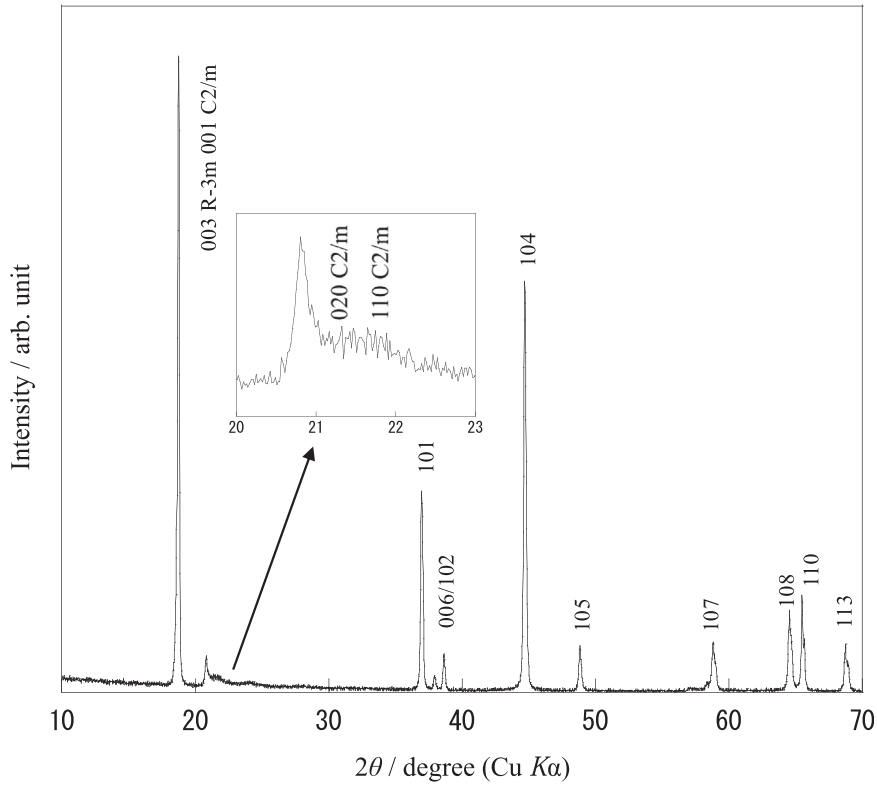


**Fig. 1.** Powder X-ray diffraction patterns of $0.6Li_2MnO_3$–$0.4Li(Mn_{1/3}Ni_{1/3}Co_{1/3})O_2$ materials for pristine electrode.

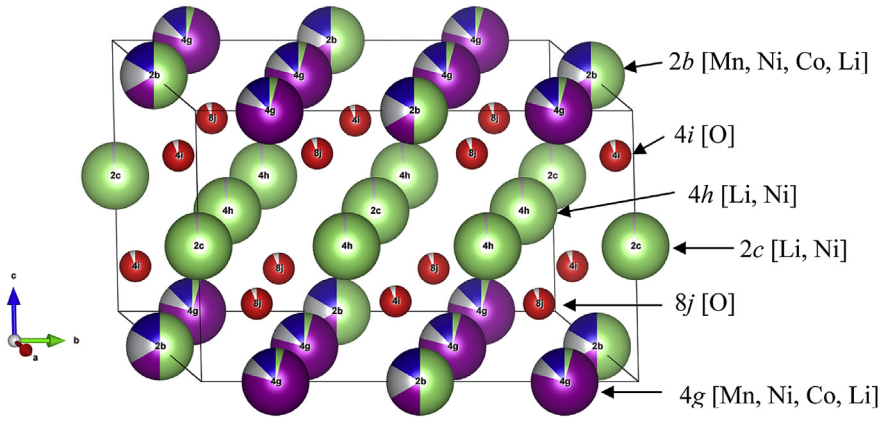


**Fig. 3.** Crystal structure model of $0.6Li_2MnO_3$–$0.4Li(Mn_{1/3}Ni_{1/3}Co_{1/3})O_2$ materials for *C2/m* model.

Neutron diffraction measurements were performed with a J-PARC iMATERIA (BL-20). The powder sample consisted of 0.8 g of active material and the measurement time was 180 min; the active-material contents of the cathodes after electrochemical measurements were approximately 8.5 mg and the measurement times were 300–330 min. The measurements for cathodes after charge or discharge were performed after stripping the Al foil current collector. Crystal structure analysis was performed with Rietveld refinement using Z-Rietveld (ver. 0.9.34) [14]. The average structures were also refined by the Rietveld analysis (RIETAN-FP ver. 1.8) [15] for the synchrotron X-ray diffractions (SPring-8, BL19B2). The electron-density distributions were evaluated by the Maximum Entropy Method (MEM) from the synchrotron XRD data using the PRIMA program (ver. 1.8) [16].

### 2.3. Electrochemical measurement

The electrochemical performances of each sample were evaluated using an HS-cell composed of the cathode, lithium anode, a Cellgard polypropylene separator, and $LiPF_6$ in 1:1 ethylene carbonate (EC)/dimethyl carbonate (DMC) as electrolyte. The cathode was prepared by mixing 80 wt % sample with 10 wt % acetylene black and 10 wt % PVdF (polyvinylidene difluoride) binder; the mixture was rolled into thin aluminum sheets that were punched into 1 cm diameter circular disks. The electrodes were pressed at 40 MPa and dried at 110 °C for 24 h under a vacuum atmosphere. All cells were fabricated in an argon-filled glove box. The cells were aged for 24 h before charge/discharge to ensure full absorption of the electrolyte into the electrode. The cells were galvanostatically cycled at room temperature at a low current density of 20 mA $g^{-1}$ (about 0.1 C rate) in an Hokuto Denko (HJR-1010mSM8) tester. The voltage was limited between 4.8 V and 2.5 V *v.s.* $Li/Li^+$, with an open circuit interval of 2 min between each charge and discharge.

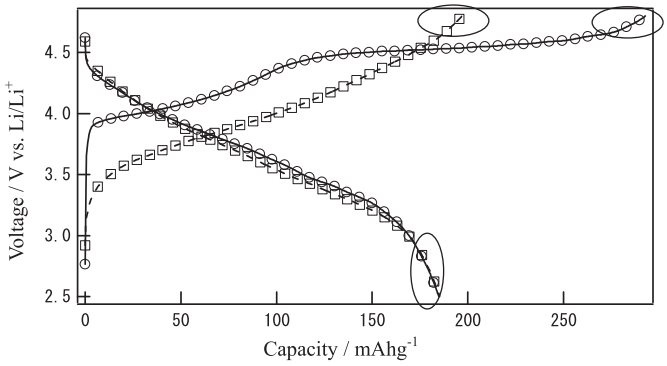


**Fig. 4.** Charge–discharge profiles for the 1st and 5th cycles of $0.6Li_2MnO_3$–$0.4Li(Mn_{1/3}Ni_{1/3}Co_{1/3})O_2$. (Temperature: 25 °C, current density: 20 mA $g^{-1}$, cut off voltage: 2.5–4.8 V *v.s.* $Li/Li^+$) ○: first cycle □: fifth cycle.

## 3. Results and discussion

### 3.1. Characterization and electrochemical property

Fig. 1 shows the powder XRD patterns for the $0.6Li_2MnO_3$–$0.4Li(Mn_{1/3}Ni_{1/3}Co_{1/3})O_2$, which was prepared by the co-

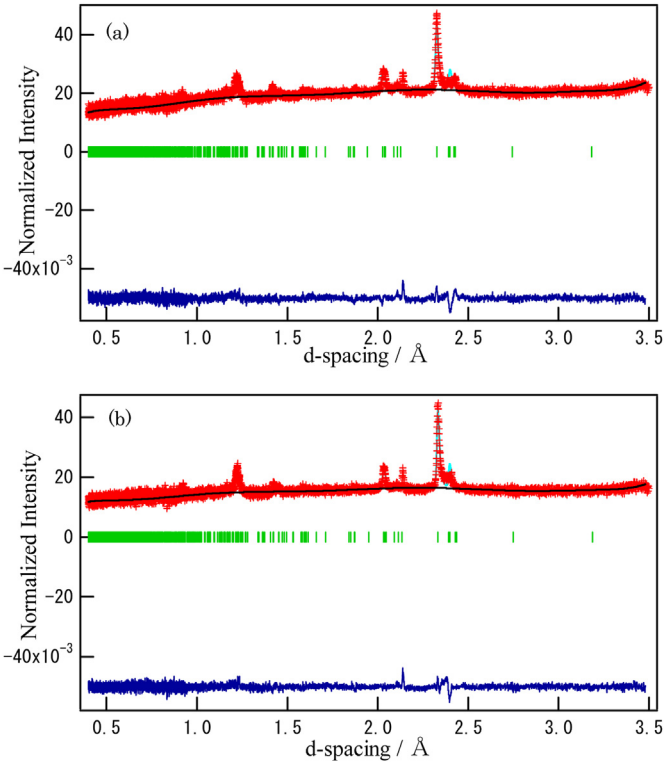


**Fig. 5.** Rietveld refinement patterns of (a) fifth charged sample (b) fifth discharged sample in space group *C2/m*. Plus marks show observed neutron diffraction intensities and a solid line represents calculated intensities. The vertical marks indicate positions of allowed Bragg reflections. The curve at the bottom is a difference between the observed and calculated intensities in the same scale.

**Table 1**
Final results of Rietveld refinements for $0.6Li_2MnO_3$–$0.4Li(Mn_{1/3}Ni_{1/3}Co_{1/3})O_2$ materials in space group $C2/m$ at room temperature. $B$ is an isotropic thermal parameter. Numbers in parentheses are estimated standard deviations of the last significant digits, and parameters without deviations are fixed. $R$-factors: $R_{wp} = 5.23\%$, $R_p = 4.44\%$, $R_e = 2.26\%$, $S = 2.31$. Lattice parameters: $a = 0.49415(1)$ nm, $b = 0.85518(2)$ nm, $c = 0.502758(5)$ nm, $\beta = 109.228(2)^\circ$.

| Atoms | Site | $x$ | $y$ | $z$ | $B \times 10^2$ (nm$^2$) | Site occupancy |
|---|---|---|---|---|---|---|
| Li1 | 4*g* | 0 | 0.1693(7) | 0 | 0.08(4) | 0.036(2) |
| Mn1 | 4*g* | =Li1($x$) | =Li1($y$) | =Li1($z$) | =Li1($B$) | 0.756(3) |
| Ni1 | 4*g* | =Li1($x$) | =Li1($y$) | =Li1($z$) | =Li1($B$) | 0.092(1) |
| Co1 | 4*g* | =Li1($x$) | =Li1($y$) | =Li1($z$) | =Li1($B$) | 0.115(1) |
| Li2 | 2*b* | 0 | 1/2 | 0 | 0.1 | 0.500(3) |
| Mn2 | 2*b* | =Li2($x$) | =Li2($y$) | =Li2($z$) | =Li2($B$) | 0.162(6) |
| Ni2 | 2*b* | =Li2($x$) | =Li2($y$) | =Li2($z$) | =Li2($B$) | 0.171(1) |
| Co2 | 2*b* | =Li2($x$) | =Li2($y$) | =Li2($z$) | =Li2($B$) | 0.166(2) |
| Li3 | 2*c* | 0 | 0 | 1/2 | 1.4(3) | 0.982(4) |
| Ni3 | 2*c* | =Li3($x$) | =Li3($y$) | =Li3($z$) | =Li3($B$) | 0.018(4) |
| Li4 | 4*h* | 0 | 0.6613(8) | 1/2 | 0.9(1) | 0.989(2) |
| Ni4 | 4*h* | =Li4($x$) | =Li4($y$) | =Li4($z$) | =Li4($B$) | 0.011(2) |
| O1 | 4*i* | 0.2218(6) | 0 | 0.2239(4) | 0.35(4) | 0.932(6) |
| O2 | 8*j* | 0.2500(4) | 0.3229(1) | 0.2228(2) | 0.48(2) | 0.938(4) |

**Table 2**
Final results of Rietveld refinements for the electrode after fifth charge in space group $C2/m$ at room temperature. $B$ is an isotropic thermal parameter. Numbers in parentheses are estimated standard deviations of the last significant digits, and parameters without deviations are fixed. $R$-factors: $R_{wp} = 4.44\%$, $R_p = 3.76\%$, $R_e = 3.35\%$, $S = 1.32$. Lattice parameters: $a = 0.4928(1)$ nm, $b = 0.8511(2)$ nm, $c = 0.50853(7)$ nm, $\beta = 109.16(1)^\circ$.

| Atoms | Site | $x$ | $y$ | $z$ | $B \times 10^2$ (nm$^2$) | Site occupancy |
|---|---|---|---|---|---|---|
| Li1 | 4*g* | 0 | 0.165(7) | 0 | 0.248 | 0.07(1) |
| Mn1 | 4*g* | =Li1($x$) | =Li1($y$) | =Li1($z$) | =Li1($B$) | 0.77(3) |
| Ni1 | 4*g* | =Li1($x$) | =Li1($y$) | =Li1($z$) | =Li1($B$) | 0.04(1) |
| Co1 | 4*g* | =Li1($x$) | =Li1($y$) | =Li1($z$) | =Li1($B$) | 0.10(1) |
| Li2 | 2*b* | 0 | 1/2 | 0 | 0.10 | 0.29(3) |
| Mn2 | 2*b* | =Li2($x$) | =Li2($y$) | =Li2($z$) | =Li2($B$) | 0.13(7) |
| Ni2 | 2*b* | =Li2($x$) | =Li2($y$) | =Li2($z$) | =Li2($B$) | 0.17(1) |
| Co2 | 2*b* | =Li2($x$) | =Li2($y$) | =Li2($z$) | =Li2($B$) | 0.17(3) |
| Li3 | 2*c* | 0 | 0 | 1/2 | 1.82 | 0.19(3) |
| Ni3 | 2*c* | =Li3($x$) | =Li3($y$) | =Li3($z$) | =Li3($B$) | 0.14(3) |
| Li4 | 4*h* | 0 | 0.66(2) | 1/2 | 0.354 | 0.34(1) |
| Ni4 | 4*h* | =Li4($x$) | =Li4($y$) | =Li4($z$) | =Li4($B$) | 0.00(1) |
| O1 | 4*i* | 0.234(6) | 0 | 0.203(4) | 0.1 | 0.87(7) |
| O2 | 8*j* | 0.239(4) | 0.324(1) | 0.219(2) | 0.179 | 0.87(5) |

**Table 3**
Final results of Rietveld refinements for the electrode after fifth discharge in space group $C2/m$ at room temperature. $B$ is an isotropic thermal parameter. Numbers in parentheses are estimated standard deviations of the last significant digits, and parameters without deviations are fixed. $R$-factors: $R_{wp} = 5.14\%$, $R_p = 4.38\%$, $R_e = 4.14\%$, $S = 1.24$. Lattice parameters: $a = 0.4942(1)$ nm, $b = 0.8541(3)$ nm, $c = 0.50810(8)$ nm, $\beta = 109.13(2)^\circ$.

| Atoms | Site | $x$ | $y$ | $z$ | $B \times 10^2$ (nm$^2$) | Site occupancy |
|---|---|---|---|---|---|---|
| Li1 | 4*g* | 0 | 0.165(7) | 0 | 0.248 | 0.03(1) |
| Mn1 | 4*g* | =Li1($x$) | =Li1($y$) | =Li1($z$) | =Li1($B$) | 0.77(3) |
| Ni1 | 4*g* | =Li1($x$) | =Li1($y$) | =Li1($z$) | =Li1($B$) | 0.080(9) |
| Co1 | 4*g* | =Li1($x$) | =Li1($y$) | =Li1($z$) | =Li1($B$) | 0.10(1) |
| Li2 | 2*b* | 0 | 1/2 | 0 | 0.10 | 0.39(3) |
| Mn2 | 2*b* | =Li2($x$) | =Li2($y$) | =Li2($z$) | =Li2($B$) | 0.11(7) |
| Ni2 | 2*b* | =Li2($x$) | =Li2($y$) | =Li2($z$) | =Li2($B$) | 0.17(1) |
| Co2 | 2*b* | =Li2($x$) | =Li2($y$) | =Li2($z$) | =Li2($B$) | 0.18(3) |
| Li3 | 2*c* | 0 | 0 | 1/2 | 1.82 | 0.57(2) |
| Ni3 | 2*c* | =Li3($x$) | =Li3($y$) | =Li3($z$) | =Li3($B$) | 0.06(2) |
| Li4 | 4*h* | 0 | 0.66(2) | 1/2 | 0.354 | 0.64(1) |
| Ni4 | 4*h* | =Li4($x$) | =Li4($y$) | =Li4($z$) | =Li4($B$) | 0.00(1) |
| O1 | 4*i* | 0.234(6) | 0 | 0.203(4) | 0.1 | 0.87(7) |
| O2 | 8*j* | 0.239(4) | 0.324(1) | 0.219(2) | 0.179 | 0.87(4) |

precipitation method. Layered structures were confirmed by the peak splitting of the (006)/(102) and (108)/(110). Although the main peaks were attributed to the layered rock-salt structure, α-$NaFeO_2$ (S.G.: $R\bar{3}m$), the broad peaks from 20° to 23° were assigned to the $C2/m$ structure [8–11,17]. The previous studies using HR-TEM and structural simulation suggested that the stacking fault resulted in the peak broadening [8–11]. The metallic composition determined by ICP was $Li_{1.18}Mn_{0.56}Ni_{0.13}Co_{0.13}O_2$ and coincided closely with the nominal compositions. The charge–discharge curves were characterized by the voltage plateau at about 4.5 V as confirmed by several lithium-rich layered materials. Fig. 2 shows the d$Q$/d$V$ profiles of the cell, and the peak at 3.3 V was attributed to the $Mn^{4+}$/$Mn^{3+}$ reduction due to the generation of electrochemically active $MnO_2$ [1].

### 3.2. Average structural analysis by neutron diffraction

Rietveld analysis based on the neutron diffraction of the $0.6Li_2MnO_3$–$0.4Li(Mn_{1/3}Ni_{1/3}Co_{1/3})O_2$ was performed to reveal the average structures during the charge–discharge cycles. While almost all peaks were indexed by the $R\bar{3}m$, most of the peaks were attributed to the $Li_2MnO_3$ type structure. Thus, the crystal structure was analyzed as the $C2/m$ space group (Fig. 3). This study

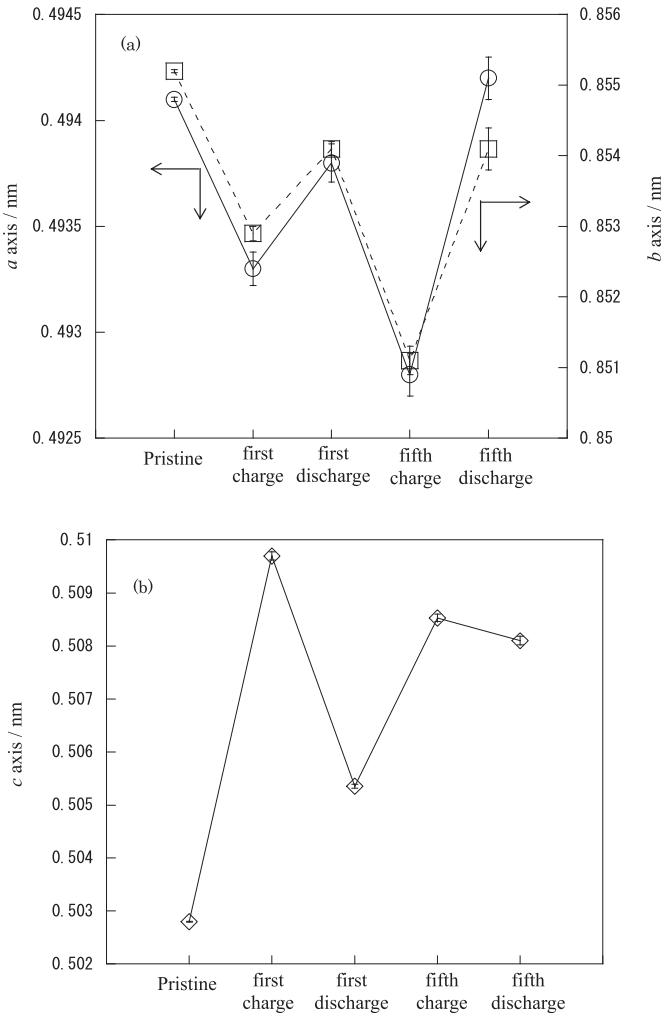


**Fig. 6.** Change of lattice parameters for (a) $a$, $b$ axis and (b) $c$ axis. ○: $a$ axis, □: $b$ axis, ◊: $c$ axis.

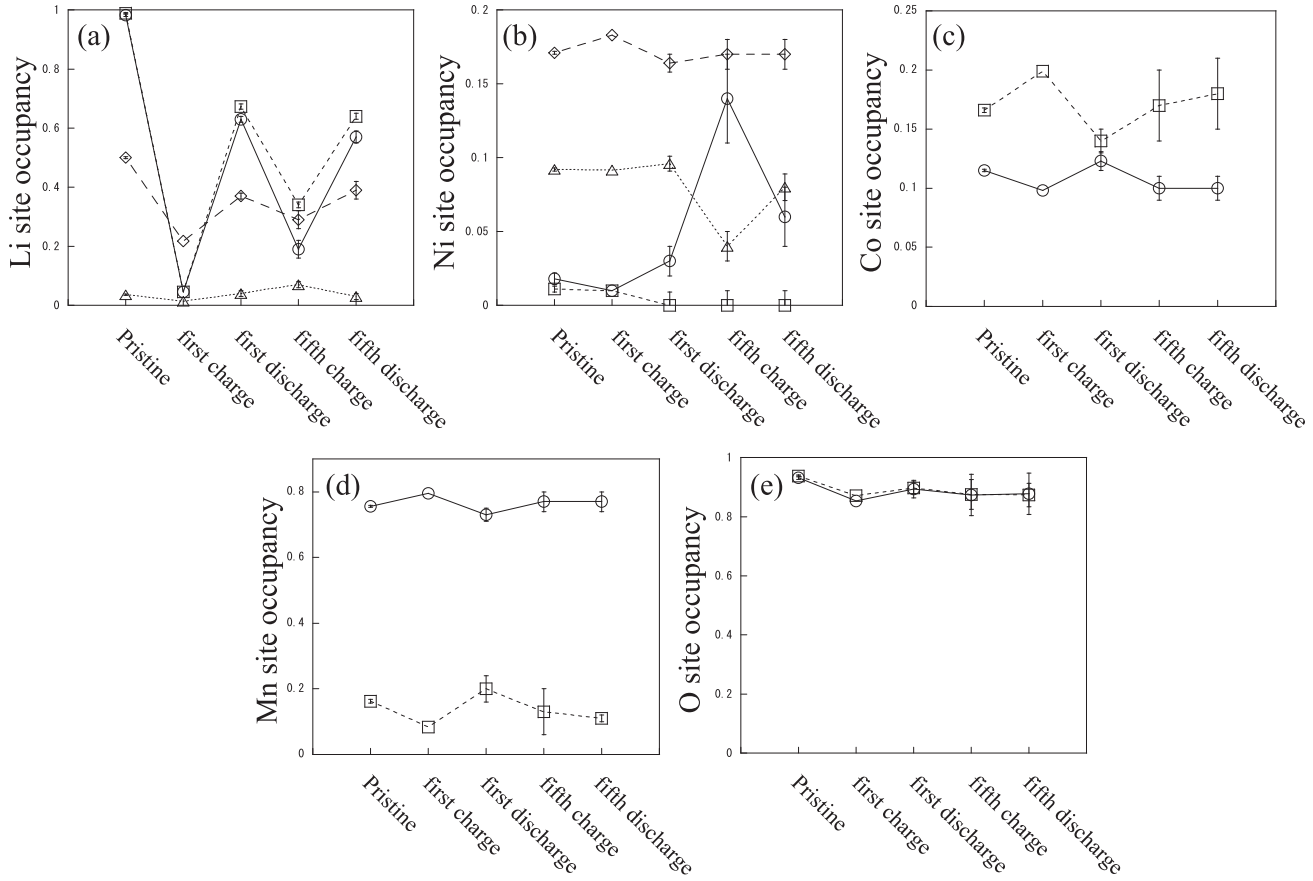


**Fig. 7.** Change of the site occupancies at (a) Li, (b) Ni, (c) Co, (d) Mn and (e) O sites. ○: 2*c* site, □: 4*h* site, Δ: 4*g* site, ◊: 2*b* site in (a) and (b), ○: 4*g* site, □: 2*b* site in (c) and (d), ○: 4*i* site, □: 8*j* site in (e).

investigated the average structure for the following four electrochemical conditions: after the first charge, after the first discharge, after the fifth charge and after the fifth discharge (Fig. 4). After the fifth cycle, the structure was regarded as stable because of the monotonous d*Q*/d*V* profiles. The total occupancies of Mn, Ni and Co were fixed as the amount determined by ICP analysis and of Li was evaluated by the specific capacities during the charge and discharge. The cation mixing was considered such that the Ni ions partially occupied the Li layer, *i.e.*, the 2*c* and 4*h* sites. When the refined parameter converged at an unusual value, the fixed parameters were used. Examples for the time of flight neutron analysis (iMATERIA) for the electrodes after the fifth cycle are shown in Fig. 5. The obtained structural parameters are summarized in Tables 1–3. The lattice parameters and occupancies of all the present data are shown in Figs. 6 and 7. Recent STEM studies [18,19] showed local structure and structural change after charging the $Li_2MnO_3$–$LiMO_2$ (M: Mn, Ni, Co). Although the present work tried to detect the spinel structure using neutron diffraction, enough intensity of neutron diffraction peaks were not obtained to detect the spinel structure in this study. Therefore the present study analyzed the neutron diffraction patters for the mono-phase with *C*2/*m* space group. The larger cell, *e.g.* laminated-type cell, including over 100 mg active material would be required for future work.

**Table 5**
Distortion of 4*g*-8*j*, 4*g*-4*i*, 2*b*-8*j*, 2*b*-4*i* and 4*h*-8*j*, 4*h*-4*i*, 2*c*-8*j*, 2*c*-4*i* octahedral in space group *C*2/*m* of electrodes after charge.

| Sample | 4*g*-8*j*, 4*g*-4*i* | | 2*b*-8*j*, 2*b*-4*i* | | 4*h*-8*j*, 4*h*-4*i* | | 2*c*-8*j*, 2*c*-4*i* | |
|---|---|---|---|---|---|---|---|---|
| | $\lambda$ | $\sigma^2$ (deg$^2$) | $\lambda$ | $\sigma^2$ (deg$^2$) | $\lambda$ | $\sigma^2$ (deg$^2$) | $\lambda$ | $\sigma^2$ (deg$^2$) |
| Pristine | 1.004 | 13.81 | 1.010 | 33.07 | 1.010 | 33.80 | 1.010 | 34.71 |
| First charge | 1.009 | 28.62 | 1.006 | 16.46 | 1.020 | 61.32 | 1.018 | 66.91 |
| First discharge | 1.008 | 24.95 | 1.012 | 30.84 | 1.015 | 54.96 | 1.010 | 31.58 |
| Fifth charge | 1.007 | 21.25 | 1.010 | 32.06 | 1.017 | 61.83 | 1.012 | 39.08 |
| Fifth discharge | 1.007 | 22.98 | 1.010 | 26.46 | 1.017 | 61.26 | 1.008 | 27.61 |

**Table 4**
The bond length in space group *C*2/*m* of the electrodes after charge.

| Sample | Bond length (nm) | | | | | | | | | |
|---|---|---|---|---|---|---|---|---|---|---|
| | 4*g*-8$j_1$ | 4*g*-8$j_2$ | 4*g*-4*i* | 2*b*-8*j* | 2*b*-4*i* | 4*h*-8$j_1$ | 4*h*-8$j_2$ | 4*h*-4*i* | 2*c*-8*j* | 2*c*-4*i* |
| Pristine | 0.1896(1) | 0.1923(14) | 0.1970(6) | 0.20404(9) | 0.2044(3) | 0.2150(1) | 0.20602(9) | 0.21125(7) | 0.21513(9) | 0.2032(2) |
| First charge | 0.1964(14) | 0.2038(14) | 0.1965(10) | 0.1965(10) | 0.181(2) | 0.2026(13) | 0.2079(14) | 0.2160(11) | 0.2094(14) | 0.226(2) |
| First discharge | 0.1881(8) | 0.1980(8) | 0.1925(8) | 0.2077(9) | 0.184(2) | 0.2098(8) | 0.1980(8) | 0.2188(8) | 0.2164(8) | 0.2246(13) |
| Fifth charge | 0.1967(13) | 0.1883(12) | 0.2004(9) | 0.1935(13) | 0.1793(13) | 0.2206(11) | 0.2107(12) | 0.2152(12) | 0.2116(12) | 0.2288(13) |
| Fifth discharge | 0.1896(6) | 0.1984(7) | 0.1919(6) | 0.2060(7) | 0.1887(12) | 0.2088(6) | 0.1970(6) | 0.2260(6) | 0.2165(6) | 0.2202(10) |

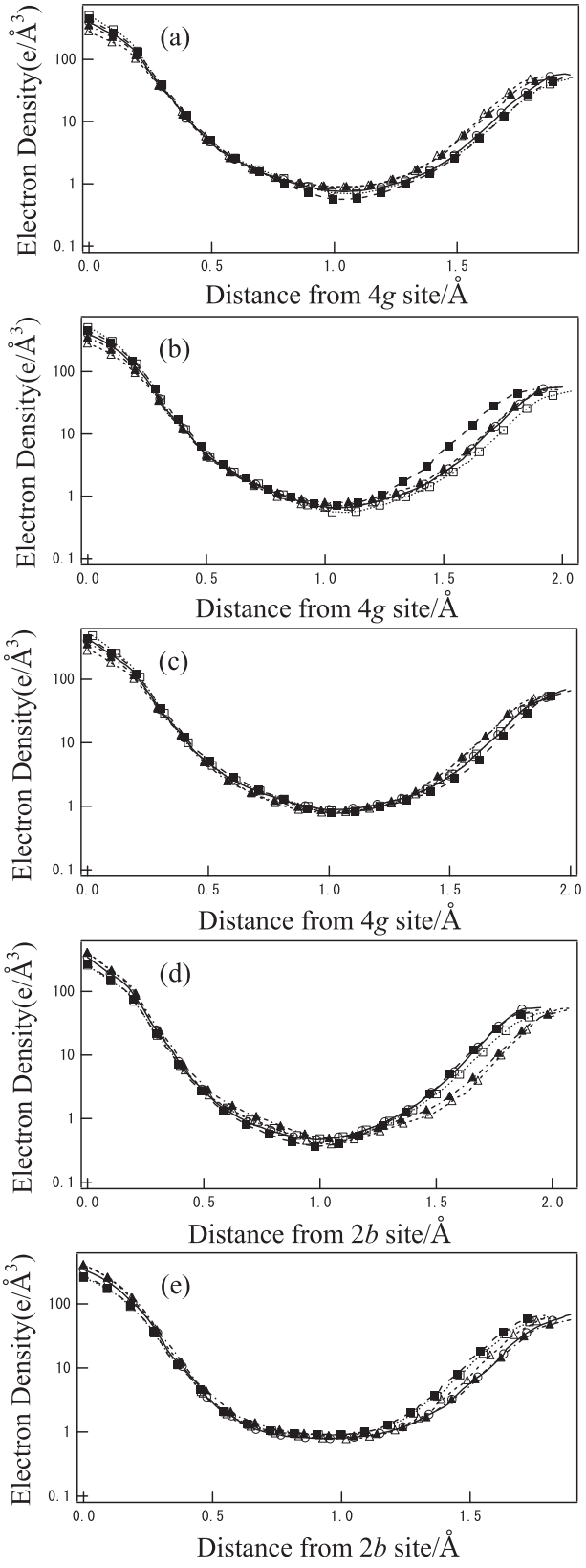


**Fig. 8.** Line profiles of electron densities between (a) 4g-8$j_1$, (b) 4g-8$j_2$, (c) 4g-4*i*, (d) 2*b*-8*j*, and (e) 2*b*-4*i* of charged samples calculated by PRIMA. ○: pristine, □: first charge, Δ: first discharge, ■: fifth charge, ▲: fifth discharge.

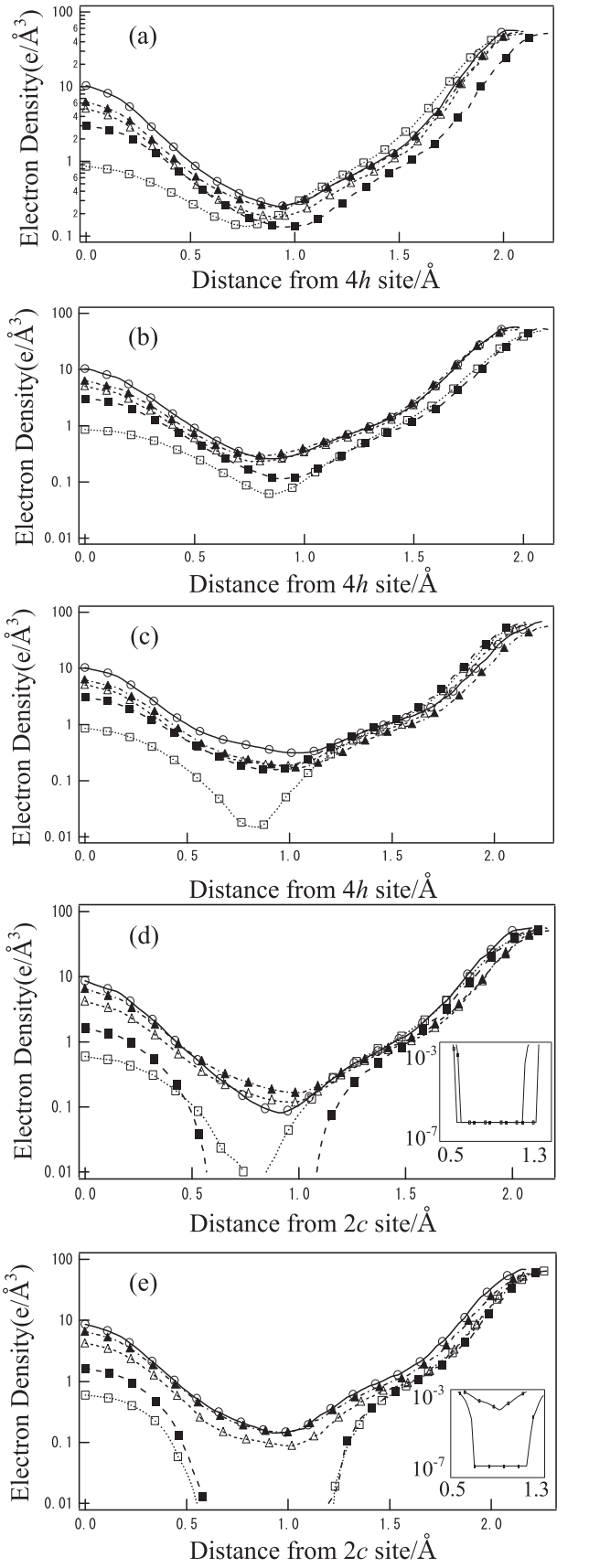


**Fig. 9.** Line profiles of electron densities between (a) 4*h*-8$j_1$, (b) 4*h*-8$j_2$, (c) 4*h*-4*i*, (d) 2*c*-8*j*, and (e) 2*c*-4*i* of charged samples calculated by PRIMA. ○: pristine, □: first charge, Δ: first discharge, ■: fifth charge, ▲: fifth discharge.

The lattice constants of the *a* and *b* axes decreased after the charge process and increased after the discharge, whereas the *c* axis increased after the charge process. The stretchings of the *a* and *b* axes were due to the difference in the ionic radii of the transition metal ions in their oxidation states. On the other hand, the *c* axis was elongated by the O–O repulsion in the charged state because of the deficiency of lithium ions in the lithium layer.

The results of the refined occupancy revealed that the lithium ions were extracted during charge process both from the transition-metal layers, the 4*g* and 2*b* sites, and from the lithium ion layers, the 2*c* and 4*h* sites. Especially, the preferred extraction of lithium was observed in the 2*b* site. The Li/Ni cation mixing at the 2*c* site in the lithium layer increased at the fifth cycle rather than the first cycle. While Co was transferred from the 4*g* to 2*b* site after the charge process and to the 4*g* site after the discharge process, the Mn ions underwent the opposite effect. Thus, the movement from site to site in the transition metal layer was revealed for Mn and Co. Reversible migration of transition metals and Li in transition metal layers was consistent with STEM results [18] and the result of $Li_2MnO_3$ [20]. The oxygen occupancy decreased after charge and tended to slightly reverse after discharge. The oxygen deficient after charge was consistent with the previous neutron study for $Li(Ni_{0.2}Li_{0.2}Mn_{0.6})O_2$ [21].

Tables 4 and 5 show the bond distances and the distortions of the $M-O_6$ octahedra, $\lambda$ and $\sigma^2$ [22]. The 4*h*-8$j_1$ and 4*g*-8$j_1$ represent shorter bonds than 4*h*-8$j_2$ and 4*g*-8$j_2$, respectively. While the increase of the bond distances in 4*g*-8$j_1$, 4*g*-8$j_2$ and 4*g*-4*i* were confirmed in the electrode after charging, decreases in 2*b*-8*j* and 2*b*-4*i* were observed. The distortion of the $M-O_6$ octahedra increased after the first charge and discharge. At the fifth cycle, this trend gradually disappeared.

### 3.3. Electronic structure

The electronic structure was analyzed by the Maximum Entropy Method of the synchrotron X-ray radiation powder diffraction data. The electron density profiles along several directions are shown in Figs. 8 and 9. Fig. 9 also showed enlarged view in the electron density because of extremely minor electron. The electron density in the transition metal layers, *i.e.*, 4*g* and 2*b* sites, showed no change between the pristine electrode and the electrode after discharge, while in the lithium layers, 2*c* and 4*h*, significant changes occurred. The covalency at 2*c*-4*i*, 2*c*-8*j*, 4*h*-4*i* and 4*h*-8*j* of the electrode decreased after charging to 4.8 V from the pristine and the discharge electrodes. This reduction was considered to be due to more mixing of Ni at the 2*c* site than at the 4*h* site. Since the covalency of the electrode at 4*h*-4*i* and 4*h*-8*j* after charging at the fifth cycle was greater than that after the first charge, the Li at the 4*h* site for the 5th cycle should not be extracted compared to the 1st cycle (Fig. 7). The correlation, however, between the electron density and bond distance was not mainly observed due to the slight difference in covalency.

## 4. Conclusion

The average structures of $0.6Li_2MnO_3–0.4Li(Mn_{1/3}Ni_{1/3}Co_{1/3})O_2$, which was obtained by the co-precipitation method, during charge–discharge process were investigated by the Rietveld analysis using neutron and synchrotron diffraction data. The electronic structures were analyzed by MEM using synchrotron X-ray data. The lithium extraction in the transition metal layer, *i.e.*, the 4*g* and 2*b* sites, was observed for the electrodes after charging. The Rietveld analysis of the neutron diffraction data indicated that the Li was extracted not only from the lithium layer, but also from the transition metal layer, *i.e.*, the 4*g* and 2*b* sites. The displacement of Mn and Co in the transition metal layer was confirmed such that the Co migrated from the 2*b* to 4*g* site after charging and the Mn underwent the opposite trend. The cation mixing of Ni at the 2*c* site for the fifth cycle increased compared to the first cycle. The lower covalency was confirmed at 2*c*-4*i* and 2*c*-8*j* from the MEM analysis because more cation-mixed Ni at the 2*c* site was preferable to the 4*h* site. A stronger covalency at 4*h*-4*i* and 4*h*-8*j* was found after the fifth cycle *vs.* the first cycle. Therefore, the Li at the 4*h* site was difficult to extract from the host materials.

## Acknowledgment

This work was supported by JSPS KAKENHI Grant Number 25420718 and the Tokyo Ohka Foundation for the Promotion of Science and Technology. The authors appreciate Prof. T. Ishigaki and Prof. A. Hoshikawa (Ibaraki University) for their help with the neutron diffraction measurements. The authors also acknowledge Dr. K. Osaka (Japan Synchrotron Radiation Research Institute, SPring-8) for his help with the synchrotron X-ray diffraction measurements.

## References

[1] C.S. Johnson, J.-S. Kim, C. Lefief, N. Li, J.T. Vaughey, M.M. Thackeray, Electrochem. Commun. 6 (2004) 1085.
[2] Y.J. Park, Y.-S. Hong, X. Wu, M.G. Kim, K.S. Ryu, S.H. Chang, J. Electrochem. Soc. 151 (2004) A720.
[3] N. Kumagai, J.-M. Kim, S. Tsuruta, Y. Kadoma, K. Ui, Electrochim. Acta 53 (2008) 5287.
[4] N. Tran, L. Croguennec, M. Menetrier, F. Weill, Ph Biensan, C. Jordy, C. Delmas, Chem. Mater. 20 (2008) 4815.
[5] M.M. Thackeray, C.S. Johnson, J.T. Vaughey, N. Li, S.A. Hackney, J. Mater. Chem. 15 (2005) 2257.
[6] T.A. Arunkumar, Y. Wu, A. Manthiram, Chem. Mater. 19 (2007) 3067.
[7] A. Ito, D. Li, Y. Ohsawa, Y. Sato, J. Power Source 183 (2008) 344.
[8] J. Breger, M. Jiang, N. Dupre, Y.S. Meng, Y.S. Horn, G. Ceder, C.P. Grey, J. Solid State Chem. 178 (2005) 2575.
[9] A. Ito, D. Li, Y. Sato, M. Arao, M. Watanabe, M. Hatano, H. Horie, Y. Ohsawa, J. Power Sources 195 (2010) 567.
[10] J.-S. Kim, C.S. Johnson, J.T. Vaughey, M.M. Thackeray, S.A. Hackney, W. Yoon, C.P. Grey, Chem. Mater. 16 (2004) 1996.
[11] S.-H. Kang, P. Kempgens, S. Greenbaum, A.J. Kropf, K. Amine, M.M. Thackeray, J. Mater. Chem. 17 (2007) 2069.
[12] Y. Idemoto, T. Kashima, N. Kitamura, Electrochemistry 80 (2012) 791.
[13] Y. Idemoto, Y. Tsukada, N. Kitamura, Chem. Lett. 40 (2012) 168.
[14] F. Izumi, K. Momma, Solid State Phenom. 130 (2007) 15–20.
[15] R. Ohishi, M. Yonemura, Y. Nishimaki, S. Torii, A. Hoshikawa, T. Ishigaki, T. Morishima, K. Mori, T. Kamiyama, Nucl. Instrum. Methods Phys. Res. Sect. A 600 (2009) 94.
[16] F. Izumi, R.A. Dilanian, Recent Research Developments in Physics, vol. 3, Transworld Research Network, Trivandrum, 2002, p. 699. Part II.
[17] C. Delmas, I. Saadoune, J. Power Sources 43 (1993) 593.
[18] A. Ito, K. Shoda, Y. Sato, M. Hatano, H. Horie, Y. Ohsawa, J. Power Sources 196 (2011) 4785.
[19] K.A. Jarvis, Z. Deng, L.F. Allard, A. Manthiram, P.J. Ferreira, Chem. Mater. 23 (2011) 3614.
[20] A.R. Armstrong, M. Holzapfel, P. Novak, C.S. Johnson, S.-H. Kang, M.M. Thackeray, P.G. Bruce, J. Am. Chem. Soc. 128 (2006) 8694.
[21] R. Wang, X. He, L. He, F. Wang, R. Xiao, L. Gu, H. Li, Adv. Energy Mater. 3 (2013) 1358.
[22] K. Robinson, G.V. Gibbs, P.H. Ribbe, Science 172 (1971) 567.